

Article

The Atmosphere's Effect on Stainless Steel Slabs' Oxide Formation in a CH₄-Fuelled Reheating Furnace

Aleksi Laukka *, Eetu-Pekka Heikkinen  and Timo Fabritius 

Process Metallurgy Group, University of Oulu, FI-90014 Oulu, Finland; eetu.heikkinen@oulu.fi (E.-P.H.); timo.fabritius@oulu.fi (T.F.)

* Correspondence: aleksi.laukka@oulu.fi; Tel.: +358-5035-19142

Abstract: Utilising the oxyfuel practice for CH₄-fuelled combustion has positive effects on the emissions, efficiency and cost of high temperature furnace practices. However, especially in older installations, oxyfuel usage requires retrofitting and alters the atmosphere in which the oxidation of the steel occurs, when compared to using air as the oxidiser. Stainless steel slab oxide growth during reheating was studied in different atmospheres. The simulated post-burn atmospheres from oxyfuel, lean oxyfuel and air-fuel practices were used to compare oxide-scale layer growth and morphology during simulated typical AISI 304 stainless steel slab reheating prior to hot rolling. Thermogravimetric measurements, glow discharge optical emission spectrometer (GDOES) and field-emission scanning electron microscope energy dispersive X-ray (FESEM-EDS) methodology were applied to discern differences between oxide growth and inner oxide layer morphology between the three practices. Switching from air to oxyfuel practice at a single temperature had the same increasing effect on the scale formation amount as a 25 °C temperature increase in air atmosphere. Inner oxide layer depth profiling revealed C, Si and Ni to be the main elements that differed between temperatures and atmospheres. A morphology study showed Si and Ni behaviour to be linked to breakaway oxidation.

Keywords: oxidation; oxyfuel; slab; stainless steel; oxide scale; morphology; reheating



Citation: Laukka, A.; Heikkinen, E.-P.; Fabritius, T. The Atmosphere's Effect on Stainless Steel Slabs' Oxide Formation in a CH₄-Fuelled Reheating Furnace. *Metals* **2021**, *11*, 621. <https://doi.org/10.3390/met11040621>

Academic Editor: Lai-Chang Zhang

Received: 5 March 2021

Accepted: 8 April 2021

Published: 12 April 2021

Publisher's Note: MDPI stays neutral with regard to jurisdictional claims in published maps and institutional affiliations.



Copyright: © 2021 by the authors. Licensee MDPI, Basel, Switzerland. This article is an open access article distributed under the terms and conditions of the Creative Commons Attribution (CC BY) license (<https://creativecommons.org/licenses/by/4.0/>).

1. Introduction

Reheat and annealing furnaces during steel manufacturing are usually fuelled by propane or methane (NG) [1–4]. Reheating furnaces contributes to a large proportion of the steel industry's energy usage and emissions, yet only around 40% of the energy from burning fuels goes to heating the steel [5]. Depending on the furnace configuration, energy losses to exhaust gas range from 13% to 43% [5,6].

Similar to the burning agent, the oxidising agent can also be varied. The most common practice is to use air [1,7,8]. Using air brings almost 80% vol. % of N₂ with it. While recuperating heat from effluent furnace gases is used to preheat the combustion air [6], nitrogen is not part of the combustion process, and heat is still wasted to heat a non-reacting ingredient. By utilising the oxyfuel practice, air is replaced with pure oxygen for the combustion. This leads to inherently lowered CO₂ [9] emissions from not using the fuel to heat nitrogen, and if effluent gas recirculation is used, to lower NO_x emissions [9]. In using oxyfuel as the oxidiser, the atmosphere resulting from the combustion is altered, and leads to an increase in water vapour content when compared to using air as the oxidiser [10].

The burner type affects the burn reaction itself and using oxyfuel practices, e.g., NO_x emissions can be significantly reduced [11,12]. Further emission reductions can be achieved from flameless oxyfuel burn [12,13] or direct flame impingement (DFI) [14,15]. While traditional air/fuel burner nozzles can be utilised for oxygen-enriched practice [16], oxyfuel practice usually requires burner retrofitting due to flue gas recirculation [17].

Additionally, the burner type for DFI is different from air/fuel, oxygen enriched air/fuel and oxyfuel burners because of the increase in nozzle jet velocity [18].

The formation and morphology of the oxide scale layer to the surface of stainless steels is affected by the atmosphere and temperature it is oxidised in. During the reheating of stainless steels slabs, the furnace temperature usually ranges from 1175 to 1250 °C [19–21] and the atmosphere depends on the fuel and oxidiser used in the heating process.

Regarding stainless steels' high temperature oxidation in oxyfuel- and oxygen-enriched atmospheres, the most common field of study is material longevity research for power plant technologies [22–30]. Firstly, the timeframe of these studies, measured at thousands of hours, differs greatly from the usual few hours required for slab/billet reheating prior to hot rolling. Secondly, the temperatures are much lower at 600 to 800 °C whereas steel reheating requires around 1200 to 1250 °C for complete precipitate dissolution and enough plasticity to hot roll it [31–33].

In reheating steel, due to the usage of excess oxidizing agent, oxygen and water vapour both affect the oxide scale formation in an increasing way [23], while increased water vapour amount has an even more drastic effect for Cr alloyed steels [30]. The distribution of oxygen and water vapour in a furnace are not equal, though. Models have shown that water vapour is distributed much more equally in a reheating furnace than oxygen [34]. As such, an increase in water vapour content in the furnace through oxyfuel burning should bring forth a more homogenous scale formation increasing effect than would an increase in oxygen content.

In this study, three different atmospheres resulting from CH₄ burned using either air or oxyfuel as the oxidiser were used to compare to the oxide scale layer growth parameters of AISI 304 austenitic stainless steel. The major changes in moving from air to purely oxygen as the oxidising agent for CH₄ combustion revolve around the reductions in greenhouse gas emissions, a worthy cause, but the change will affect the reheated steels' oxide growth. The aim of this research was to provide a viewpoint directly from the perspective of the materials' oxidation behaviour during reheating for an altered atmosphere, and how the behaviour might affect later processing steps. This research will help answer the following question: upon changing the oxidiser for a methane-fired stainless steel slab reheating furnace from air to oxygen, what effects regarding the oxide scale layers' formation properties are altered, and what are the consequences from their alterations to later processing stages?

2. Materials and Methods

The steel studied in this research was AISI 304 austenitic stainless steel with an alloy composition as presented in Table 1. The material used was a laboratory cast slab of AISI 304 that had been cut to sample pieces as per the methodology in Figure 1. The target sample size was 20 × 2 × 30 mm, with small variations between different samples. Prior to furnace tests, all sides of each sample were measured with a digital calliper from three different locations, and the average for each of the three sides was used to calculate the sample surface area.

Table 1. Chemical composition of the used AISI 304 stainless steel.

| C | Si | Mn | P | S | Cr | Ni | Mo | Ti | Nb | Co | V | W | B | Fe |
|-------|------|------|-------|-------|------|-----|-----|------|------|------|------|------|--------|------|
| 0.036 | 0.47 | 1.27 | 0.031 | 0.003 | 18.2 | 8.1 | 0.3 | 0.01 | 0.01 | 0.16 | 0.07 | 0.05 | 0.0007 | Bal. |

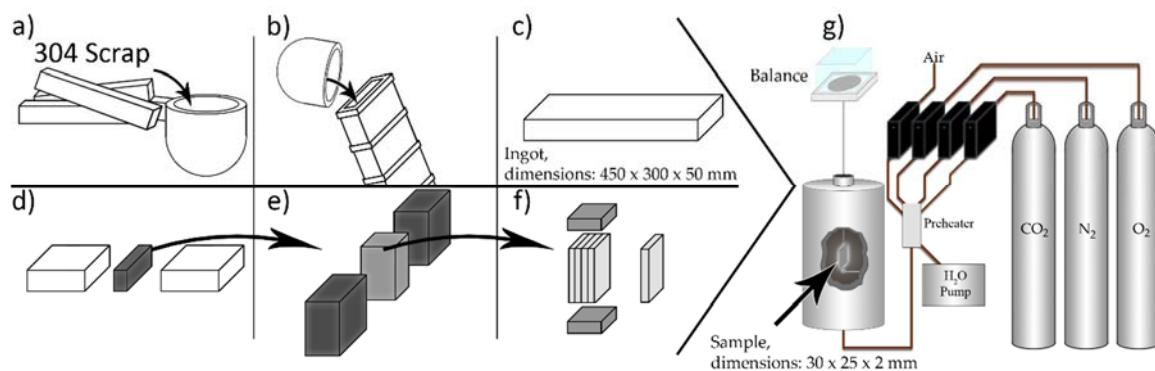


Figure 1. Sample preparation and test setup: (a) scrap pieces of AISI 304 slabs are melted in a vacuum induction furnace, (b) pouring the molten metal to a casting mould, (c) solidified laboratory slab, (d) cross sectioning of the slab, (e) further cross-sectioning from the middle of the slab, (f) slicing of the middle piece into test samples, (g) TG furnace setup with associated major components with an arrow pointing to the sample location in the furnace. Other major parts of the system are named, and the ingot and sample size are shown. Not to scale.

The thermogravimetric (TG) furnace used was a vertical tube furnace with a homogenous hot area of 35 mm at its centre. Gases were fed into the furnace through mass flow controllers that were computer controlled. The sample weight was recorded at 10 s intervals using a digital scale that was also connected to the controlling computer. The TG results were area-normalised based on the pre-measured sample surface area. The sample heating was simulated to represent the heating curve of a slab surface temperature to its target temperature in an industrial slab reheat furnace setting as per Figure 2. Due to highly deviating thermal expansion coefficients between the oxide scale and substrate metal, samples were left to cool in the TG furnace by driving down the furnace temperature. This kept the oxide scale mostly attached with the samples.

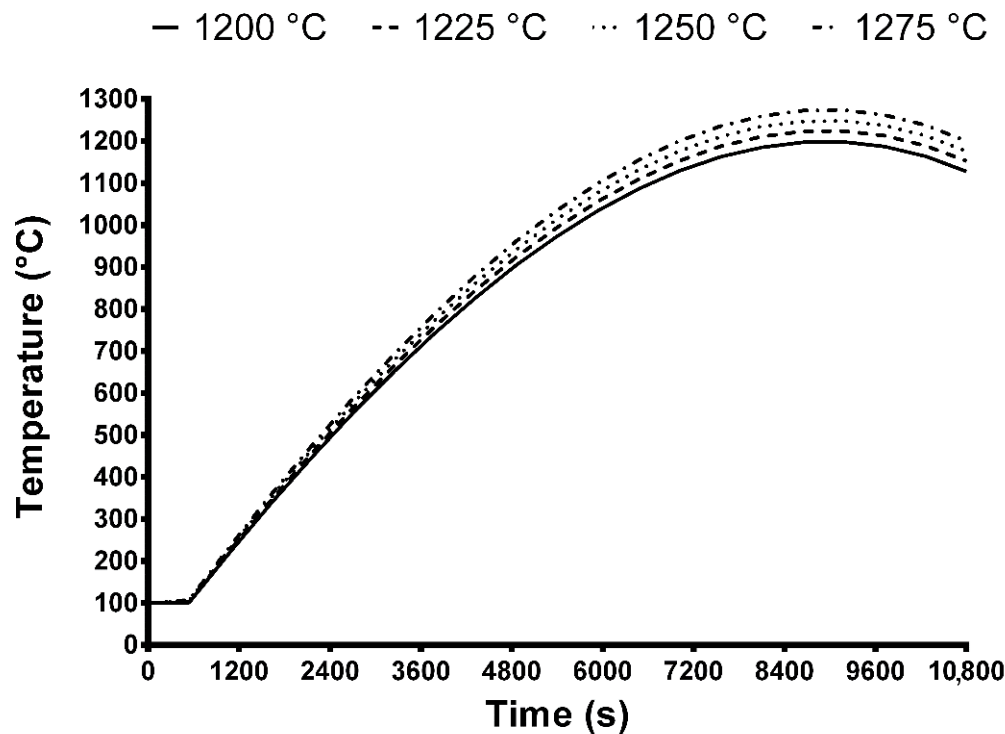


Figure 2. TG furnace heating curves.

A heating profile mimicking the slab surface temperature throughout a three-hour reheating period in an industrial walking beam furnace was utilised as the TG furnace heating profile. The heating profile curves for each of the four different temperatures in this study are presented in Figure 2. The experimental temperatures of 1200, 1225, 1250 and 1275 °C were chosen because they represent the usual operating window for the reheating of AISI 304 austenitic stainless steel slabs in an industrial setting.

After the TG tests, the samples were cold mounted in epoxy, cross-sectioned, polished and inspected with a Zeiss ULTRA plus field-emission scanning electron microscope (FESEM). An Oxford Instruments electron energy dispersive X-ray (EDS) analyser linked to the FESEM was used to gather composition information from the cross sections. A glow discharge optical emission spectrometer (GDOES) was used for the sample surfaces to analyse element depth charts and determine the inner oxide layer thickness.

The oxidiser-based differences to the atmosphere after combustion have been defined based on Equations (1) and (2). To simulate the common practice of ensuring fully burning the fuel, the used air atmosphere in Equation (1) was calculated as having the reaction happen in 20% excess air, translating the volumetric amount of excess oxygen in the post-combustion atmosphere also to oxyfuel burn, as seen in Equation (2). The exception was the lean oxyfuel atmosphere where the effect of water vapour without oxygen was studied, and the simulated post-combustion atmosphere was calculated with no excess oxygen. Thus, the square bracketed terms for oxygen in Equation (2) are considered only for the oxyfuel atmosphere. Minor constituents resulting from burning CH₄ at 1200 °C (e.g., OH, CO and H₂ ranging from 10⁻⁴ to 10⁻⁶ mol-% as calculated by GTT-Technologies' FactSage™ version 7.3) are not in the scope of this study and have been left out purposefully. The experiments' test matrix with the corresponding atmosphere compositions are shown in Table 2.



Table 2. Research experiment matrix and the compositions of the used atmospheres. For x: TG, field-emission scanning electron microscope energy dispersive X-ray (FESEM), glow discharge optical emission spectrometer (GDOES) analysis; for z: TG, FESEM analysis.

| | 1200 °C | 1225 °C | 1250 °C | 1275 °C |
|--------------|--------------------------|-------------------------------|-------------------------|-------------------------|
| Oxyfuel | x | x | x | x |
| Lean oxyfuel | x | x | x | z |
| Air | x | x | x | x |
| | CO ₂ (vol. %) | H ₂ O (g) (vol. %) | O ₂ (vol. %) | N ₂ (vol. %) |
| Oxyfuel | 32.26 | 64.52 | 3.22 | 0.00 |
| Lean oxyfuel | 33.33 | 66.67 | 0.00 | 0.00 |
| Air | 8.05 | 16.09 | 3.22 | 72.64 |

3. Results

The thermogravimetric results and GDOES depth profiles for the inner oxide layer, and the FESEM and EDS images with analyses are presented in this section. The air and oxyfuel atmosphere results are presented on the same y-axis scale, and the lean oxyfuel on a slightly lower y-axis scale in comparison to the other two. The time frame for the tests was 180 min, or 10,800 s, as the x-axis unit. The x-axis is cropped to start at 4800 s in the TG figures, as no measured oxidation happened before this point in the tests. The reason for this is seen in Figure 2: the temperature rose above the critical oxidation temperature limit only after this point. The unit for y-axis is change (increase in this case) in weight per unit area. The weight increases reported are normalised to each test samples' total area prior to the tests.

The overview FESEM back-scattered electron (BSE) images can be seen in Figure 3, and from it, it can be seen that the amount of internal oxidation is in line with the TG results; that is, the amount increases with a higher amount of mass change reported. Some of the outer oxide layer can be observed to have broken off after the TG experiments. The overall morphological differences between air and oxyfuel atmospheres were small. As the oxide layer is, in some cases, quite uneven, and consisting of clear oxide pockets, utilizing a large GDOES sputtering diameter of 4 mm was used to decrease the inherent error brought by the uneven steel–oxide layer interface when obtaining the per-element depth profiles. The uneven behaviour of oxidation under these conditions is the result of the protective Cr_2O_3 layer being sustained in most cases. Should this Cr_2O_3 layer have been annihilated, the resulting breakaway oxidation would even the steel–oxide layer interface.

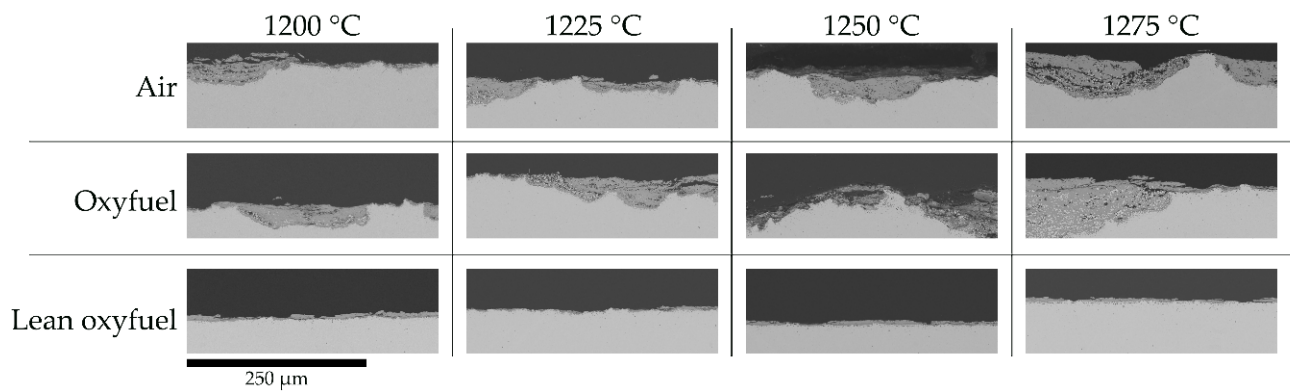


Figure 3. Overview back-scattered electron (BSE) FESEM images from the samples. Shown are the metal substrate (light grey), the attached oxide layer (medium grey), and mounting epoxy (black). Scale bar is 250 μm .

3.1. Thermogravimetric Results

As a preface, the end scaling amounts for all samples in all atmospheres are presented in Table 3. Values are shown as area normalized weight gain (kg/m^2).

Table 3. End scaling amounts of all samples for TG tests in all atmospheres, in kg/m^2 .

| | 1200 °C | 1225 °C | 1250 °C | 1275 °C |
|--------------|---------|---------|---------|---------|
| Air | 0.139 | 0.163 | 0.173 | 0.200 |
| Oxyfuel | 0.162 | 0.177 | 0.206 | 0.227 |
| Lean oxyfuel | 0.051 | 0.061 | 0.053 | 0.087 |

The TG results for mass change as a function of time for air atmosphere can be found in Figure 4. It can be observed that the overall oxide scale formation rate is similar between all the other temperatures with the exception of 1225 °C. For a period between 7100 and 8400 s in the test, it can be seen that the 1225 °C sample has a more linear oxidation behaviour when compared to the other samples in this atmosphere. While the oxidation rate for the 1200 °C sample between the same period is higher than the one at 1225 °C, the end scaling amount order increases with temperature. The point at which oxidation accelerated correlates well with the temperature, with the onset of the higher oxidation rate for 1200 °C happening at 6700 s, for 1225 °C at 6600 s, for 1250 °C at 6200 s and for 1275 °C at 6050 s.

The TG results for oxyfuel atmosphere are presented in Figure 5. The figure shows that the oxide scale formation rates were even more similar between different temperatures in this atmosphere than they were in air atmosphere. Again, the normalised oxide scale growth graphs at 1225 °C and 1200 °C intersect briefly near the 6800 s point of the test, but for a much shorter duration than they did in the air atmosphere. However, the end scaling amounts are, again, in the order of temperature. The overall per time-step oxide formation amounts were higher in the oxyfuel atmosphere than they were in the air atmosphere. The

onset of higher oxidation rates, again, correlated inversely with an increase in temperature: at 6200 s for 1200 °C, at 6000 s for 1225 °C, at 5850 s for 1250 °C and at 5650 s for 1275 °C. The time frame window between the samples' onset of the higher oxidation rate was narrower in the oxyfuel atmosphere than in the air atmosphere. The accelerated oxidation rates' onset time for an individual temperature also happened sooner than in the air atmosphere.

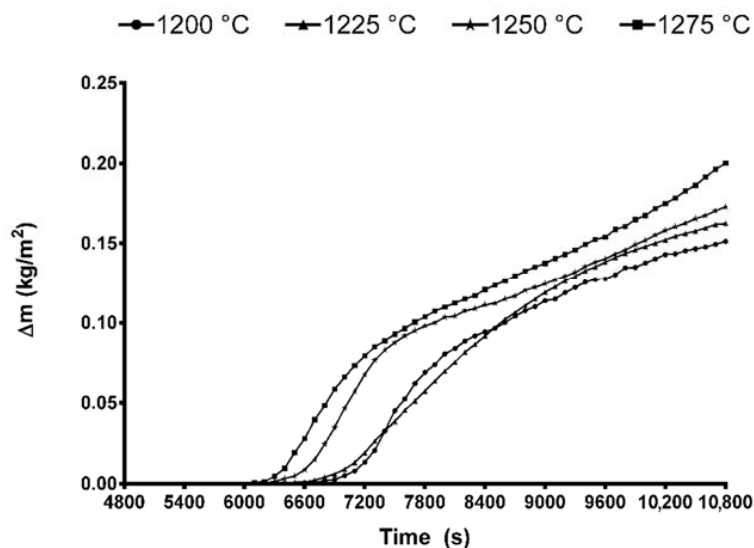


Figure 4. TG results from air atmosphere.

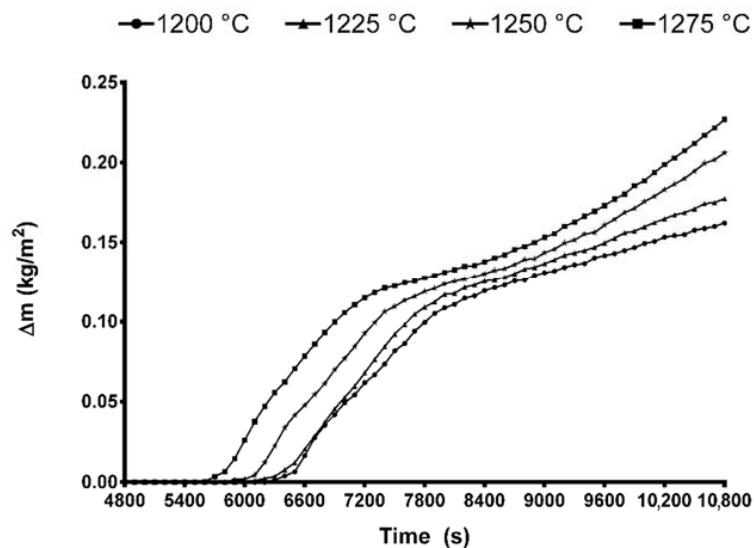


Figure 5. TG results from oxyfuel atmosphere.

The TG results for the lean oxyfuel atmosphere can be found in Figure 6. The initial beginning of rapid oxidation is very close for all other temperatures except 1275 °C, near the 6200 s mark in the test. The initial higher oxidation rate for 1275 °C began already at around the 5800 s mark. The overall shape of the area of the normalised oxide scale growth graphs appears similar for other temperatures except 1275 °C, as well. While the other temperatures show an initially fast oxidation rate between 6200 s and 8200–8400 s, followed by a diminishing oxide growth rate after it, at 1275 °C the oxide growth rate was almost linear once it had begun.

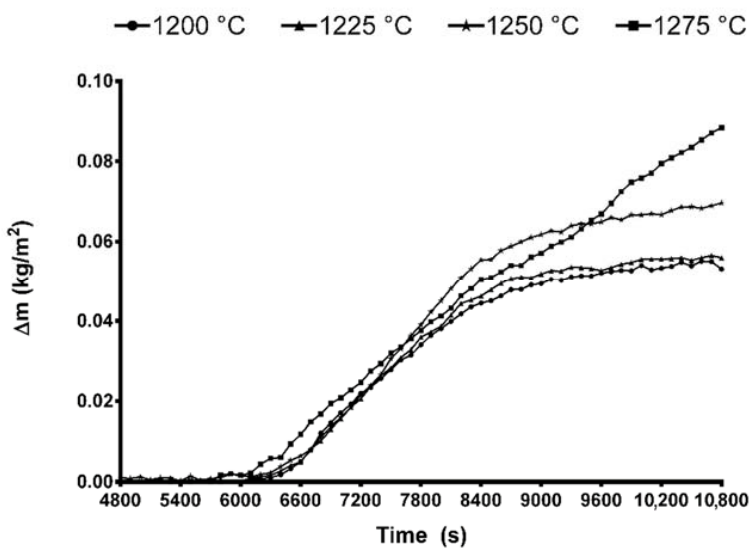


Figure 6. TG results from lean oxyfuel atmosphere.

Compared to the air and oxyfuel atmospheres, the overall oxide scale formation amount was considerably lower throughout the tests. The end scaling amounts were also only a quarter for the lean oxyfuel atmospheres than what they were for the oxyfuel experiments.

Comparing air to oxyfuel atmosphere, the time when the oxidation rate increased to an initially high rate was shortened, as seen between Figures 4 and 5. Additionally, the time frame during which the initially accelerated oxidation started to happen decreased from 650 s for air to 550 s. Additionally, the time frame during which the oxidation started to accelerate for the lean oxyfuel atmosphere was 500 s, while the individual per temperature times for the oxidation start were clustered for other temperatures except 1275 °C.

3.2. GDOES Results

As the lower temperatures' outer oxide layers' structure was flaky, and thus the thickness of the outer oxide layer varies throughout the samples' surfaces, a GDOES analysis was used to measure only the depth of the inner oxide layer. Additionally, firing the GDOES plasma through a thick outer oxide layer would decrease the accuracy of the results gained from the inner oxide layer. The GDOES depth values are indicated in μm and measured from the original sample surface. The inner oxide started at the maximum Cr value (indicative of the original sample surface) and ended when the GDOES result showed <100 ppm oxygen. The inner oxide penetration depth from the GDOES results can be seen in Table 4. The GDOES result for the lean oxyfuel sample for 1275 °C was omitted from the results because the vacuum seal on the device was imperfect, leading to erroneous results.

Table 4. GDOES measured depth for the inner oxide layer, in μm .

| | 1200 °C | 1225 °C | 1250 °C | 1275 °C |
|----------|---------|---------|---------|---------|
| Air | 46 | 48 | 55 | 77 |
| Oxy | 51 | 53 | 73 | 83 |
| Oxy lean | 13 | 19 | 23 | |

By comparing air and oxyfuel sample results, it can be seen that the penetration depth for the inner oxide layer is higher for the oxyfuel atmosphere, and the largest difference is seen at 1250 °C between these atmospheres. The lean oxyfuel atmosphere shows a much lower overall penetration depth for the inner oxide layer, being around a quarter to a third of it when compared to both air and oxyfuel atmospheres.

The depth charts from the original sample surface towards the steel substrate for the elements Fe, O, Cr, C, Mn, Si and Ni can be seen in Figure 7, indicated in wt. %. For clarity, in Figure 7, the values for carbon are increased by 100, and the values of Mn, Si and Ni are increased by 10. The data are presented unfiltered.

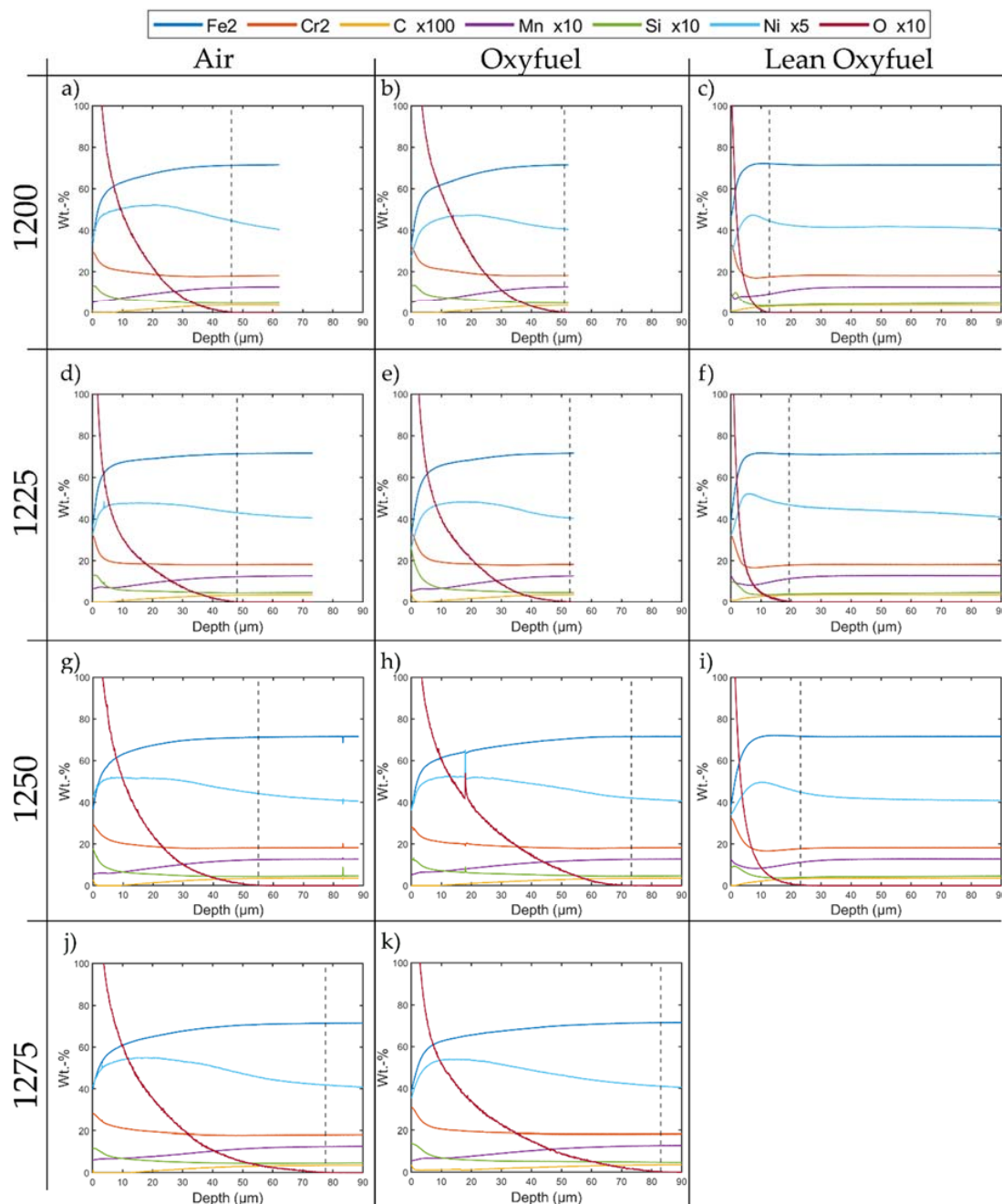


Figure 7. The GDOES depth charts in wt. % from sample surface towards the substrate metal for samples at 1200 °C in (a–c), 1225 °C in (d–f), 1250 °C in (g–i) and 1275 °C in (j–k). The x- and y-axis ranges are constant between the images, as well as the increase in values of carbon by 100 times, Mn by 10×, Si by 10× and Ni by 10×. From left to right in a single row, the order is always air, oxyfuel and lean oxyfuel atmosphere GDOES results. The vertical line in the smaller figures indicates the depth where the substrate begins.

Comparing the GDOES depth profiles of the 1200 °C samples, it can be seen that both the air and oxyfuel atmosphere samples had the Ni content rising to around 7.8 wt. % towards the depth of 20 μm from where it slowly declines. The lean oxyfuel atmosphere

had a steeper incline to the peak Ni value of 7.2 wt. % and a more rapid decline from the peak value afterwards. In addition to the steeper incline and decline for the Ni content, the lean oxyfuel atmosphere sample reached the peak Ni value sooner, at 10 µm. Overall, the differences between the air and oxyfuel atmospheres were small.

When comparing the GDOES profiles between the different atmospheres for the 1225 °C temperature, the largest differences could be found between Si and Ni profiles. Between oxyfuel and air atmospheres, the Ni content behaviour with regard to depth was slightly different to what it was at 1200 °C. In air atmosphere, the Ni content rose more rapidly to the peak value, while declining more slowly than in the oxyfuel atmosphere. Additionally, near the surface of the sample, the Si content for the oxyfuel atmosphere was almost 3 wt. % whereas for the air atmosphere it was only around 1.3 wt. %. The lean oxyfuel atmosphere showed a high nickel content peak value at 7.8 wt. %, similar to the air and oxyfuel atmospheres.

At 1250 °C, the differences between the GDOES profiles of the atmospheres were akin to the 1200 °C profiles. The largest difference with lower temperatures was the Ni behaviour of the lean oxyfuel atmosphere sample; the incline and decline from the peak nickel value were now less steep, stretching the curve in relation to the location from which the substrate begins. Air and oxyfuel atmospheres' GDOES profiles show a similar shape but the oxyfuel atmosphere follows the air atmosphere profiles in relation to the location where the substrate begins. For the oxyfuel atmosphere sample, the GDOES analysis also seems to have hit an area with a high nickel oxide zone.

Comparing different atmospheres' GDOES profiles across all temperature ranges shows that the relationships between Cr, Si and Ni are the elements contributing most to the differences between the graphs. For the differences between the oxyfuel and air atmospheres, Figure 8 shows the Ni GDOES depth profile of the (a) air and (b) oxyfuel atmospheres is limited to a depth of 60 µm. For 1200 °C, it can be seen that for the air atmosphere, the Ni peaked around 25 µm at 10.5 wt. % while the peak at the oxyfuel atmosphere was 20 µm at 9.5 wt. %. At 1225 °C, the peak for the air atmosphere was at the depth of 10 µm with 9.5 wt. % while the oxyfuel atmosphere Ni peak was at almost the same place it was at 1200 °C. For 1250 °C, the peak Ni value for air atmosphere was again at 10 µm with 10.5 wt. % and at 15 µm with around the same 10.5 wt. % for the oxyfuel atmosphere. For 1275 °C, the peak Ni value was at 18 µm with 11 wt. % for both atmospheres. For the air atmosphere, 1200 °C and 1250 °C Ni depth curves followed a rather similar path, while for the oxyfuel atmosphere, 1200 °C and 1225 °C followed each other, and 1250 °C and 1275 °C followed each other along a similar path.

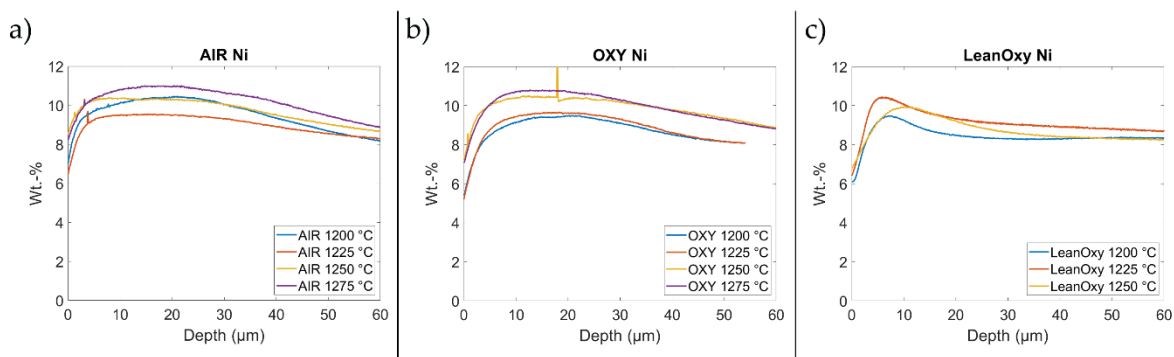


Figure 8. The individual temperature GDOES graphs for Ni in (a) air, (b) oxyfuel and (c) lean oxyfuel atmosphere.

The individual Si GDOES depth profiles for air (a) and oxyfuel (b) atmospheres can be seen in Figure 9. Differences within a single atmosphere were limited to between 0 and 30 µm. For the air atmosphere, the highest Si value was at 1250 °C at the original sample surface with 2 wt. %. The highest Si value for oxyfuel atmosphere was at 1225 °C near 3 wt. %. The other Si peaks fell between 1.2 and 1.4 wt. % for both atmospheres.

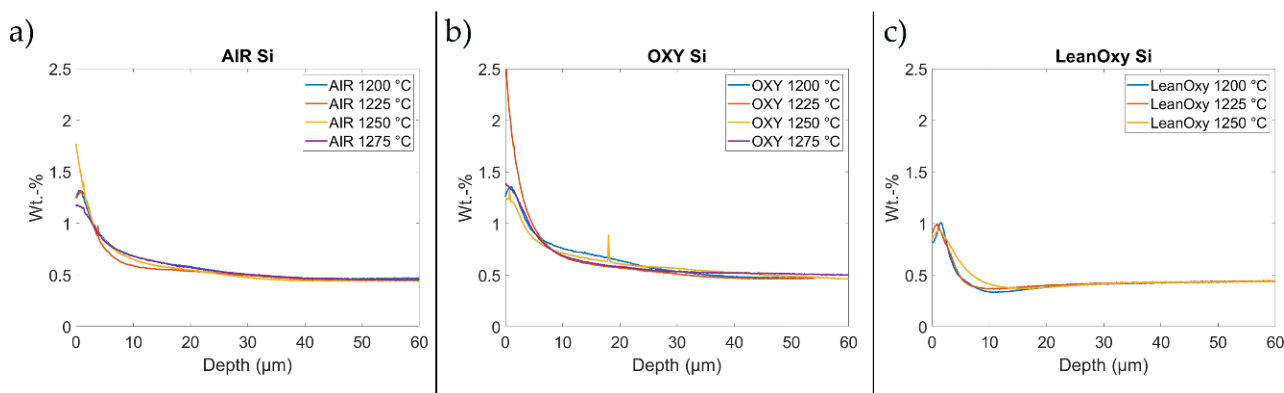


Figure 9. The individual temperature GDOES graphs for Si in (a) air, (b) oxyfuel and (c) lean oxyfuel atmosphere.

The individual Cr GDOES depth profiles for (a) air, (b) oxyfuel and (c) lean oxyfuel atmospheres can be seen in Figure 10. The overall shape of the GDOES depth profile curves in each temperature were similar between the atmospheres; that is, both 1225 °C temperature Cr depth curves show a similar sharp drop from around 33 wt. % to 19 wt. % between the first 10 μm in both atmospheres. While the wt. % curves for other temperatures between the atmospheres do not exhibit the same numbers, the shape remains similar. For the air atmosphere, the Cr depth curves of 1200 °C and 1250 °C followed each other very closely. For oxyfuel atmosphere, the 1250 °C and 1275 °C Cr depth curves followed each other closely.

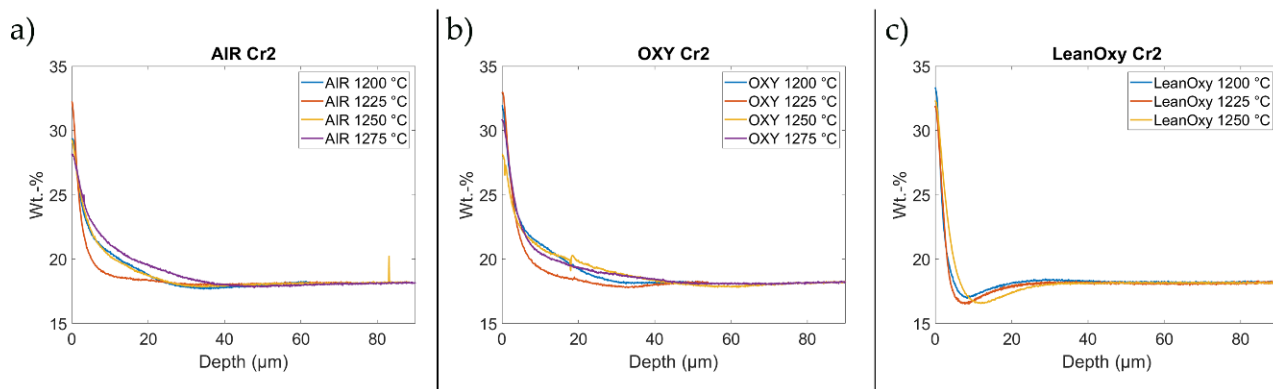


Figure 10. The individual temperature GDOES graphs for Cr in (a) air, (b) oxyfuel and (c) lean oxyfuel atmosphere.

3.3. FESEM and EDS Results

As a preface for the FESEM images, a glossary of terminology is presented in Figure 11. The terms for the parts of the sample cross-section are indicated in their respective places. The abstract terminology regarding direction of movement when reviewing the morphology is shown in directional arrows. Lastly, the original sample surface is shown as a horizontal purple line. The colours of the back-scattered electron (BSE) images are always: light grey/white: metal without oxygen; grey: Cr/Fe rich oxide; dark grey: Si rich oxide; black: pores/mounting epoxy. The EDS element maps complementing some BSE images are always colour-coded to show the relative intensity ($K\alpha 1$) of the following elements: amber: Ni; red: Si; cyan: Cr.

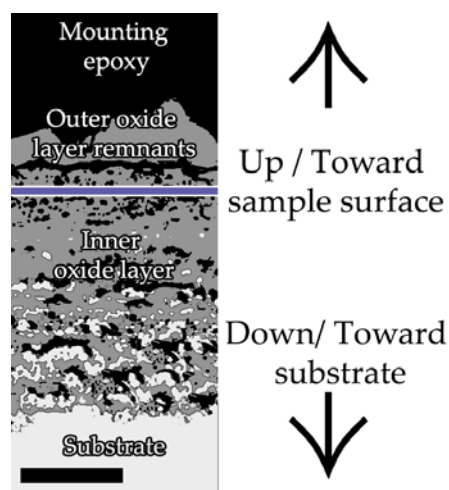


Figure 11. A modified, schematic FESEM BSE image with the substrate, inner oxide layer, outer oxide layer remnants, mounting epoxy, directions and the original sample surface marked as a horizontal purple line. Original image scale bar (black bar at the bottom of the image) is 75 μm .

The EDS analyses showed that the Si, Ni and Cr concentrations were one of the more distinct differences between the different atmospheres in each temperature. Figure 12 shows the EDS maps for Si, Ni and Cr in 1225 $^{\circ}\text{C}$ for samples in all atmospheres. It can be seen that for the air atmosphere in Figure 12a, Si could be found at the metal/oxide interface, and in large amounts in the inner oxide layer. For oxyfuel atmosphere in (b), Si was more concentrated at the metal/oxide interface, and for the lean oxyfuel atmosphere in (c), Si was found at the metal/oxide interface as a very distinct line.

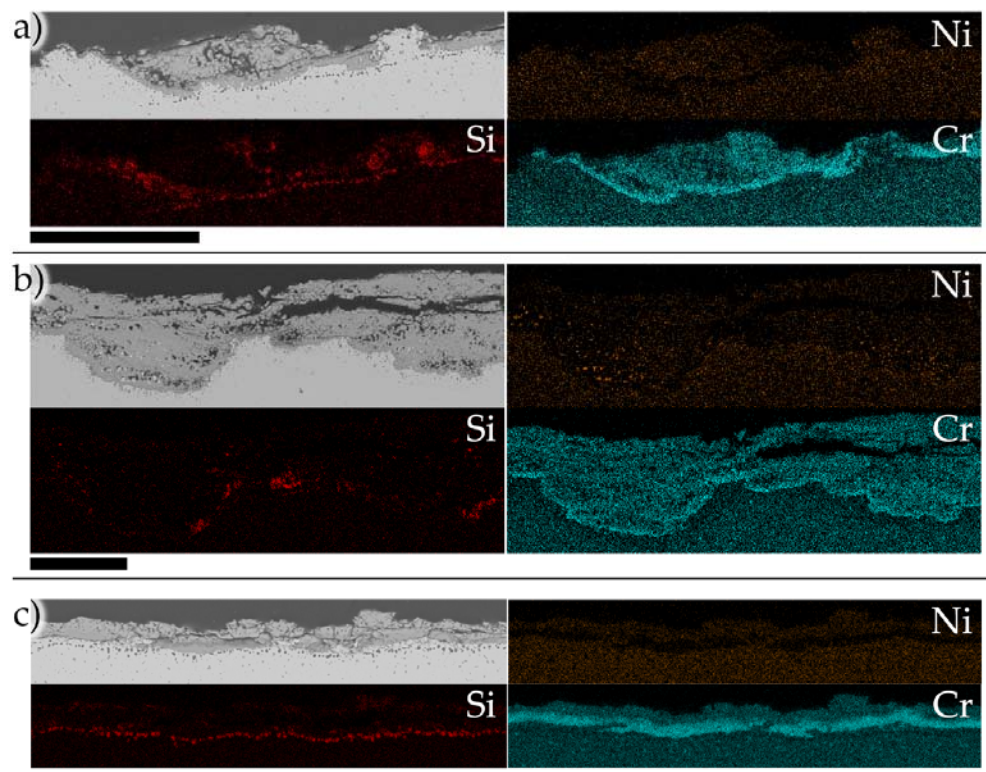


Figure 12. BSE image and corresponding energy dispersive X-ray (EDS) maps for Ni, Si and Cr in 1225 $^{\circ}\text{C}$ for (a) air atmosphere, (b) oxyfuel atmosphere and (c) lean oxyfuel atmosphere. Scale bar is 50 μm .

Comparing the Ni EDS maps in Figure 12, it can be seen that for the air atmosphere, Ni was evenly distributed in the oxide part with a Ni-free Cr layer separating the oxide and the substrate. In the oxyfuel atmosphere, there were some Ni-rich particles in the oxide, particularly near the metal/oxide interface. Near the Ni-rich particles, Ni was not found in the oxide. For the lean oxyfuel atmosphere, the Ni distribution was similar to the air atmosphere.

Comparing the Cr EDS maps in Figure 12 shows that for air atmosphere, the overall distribution of Cr was quite even, with a slightly increased Cr concentration around the areas where there were also Si-rich areas. The Cr lining between the oxide and substrate was intact. For the oxyfuel atmosphere, the distribution of Cr in the oxide was even, and the Cr lining was weakened around the areas where Ni-rich nodules were found. For the lean oxyfuel atmosphere, the Cr lining was highly visible, sandwiched between the substrate and oxide in near-identical colours. The Cr distribution in the oxide was even for the lean oxyfuel atmosphere.

Figure 13 shows the EDS maps for Ni (in amber) and Si (in red) at 1275 °C. Comparing the Si-distribution in the inner oxide layer and at the oxide/metal interface between 1275 °C and 1225 °C shows that for air (a) and oxyfuel (b) atmospheres, Si was again found at both the interface and in the inner oxide layer. For lean oxyfuel (c), Si was still localised at the metal/oxide interface and found only in small amounts in the inner oxide layer.

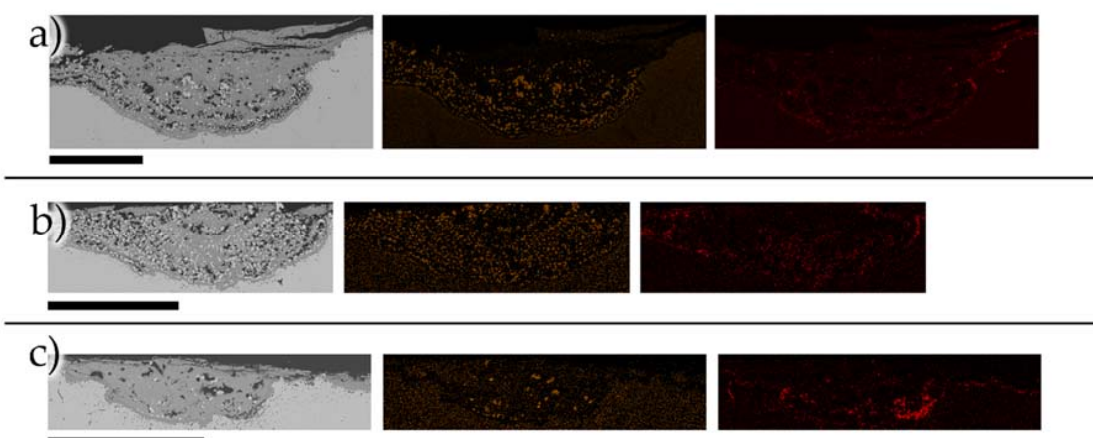


Figure 13. EDS maps for 1275 °C; (a) air, (b) oxyfuel and (c) lean oxyfuel atmospheres. Ni shown in amber, Si EDS map shown in red. Scale bar is 100 μm.

The 1275 °C samples also clearly showed the distribution of Ni particles, which contain no oxygen, in the inner oxide layer. The lean oxygen atmosphere sample in Figure 13c shows that the inner oxide layer contained only a few of these particles, while both the air and oxyfuel atmosphere samples had an even distribution of them throughout the inner oxide layer pockets.

The EDS point analysis locations from 1275 °C are presented in Figure 14 for (a) air, (b) oxyfuel and (c) lean oxyfuel atmosphere. The corresponding analyses from the locations are presented in Table 5.

Table 5. EDS point analyses corresponding to Figure 14, in wt. %. No value indicated means the element was not detected at the analysis point.

| | 1 | 2 | 3 | 4 | 5 | 6 | 7 | 8 | 9 | 10 | 11 | 12 | 13 |
|-------|-----|-----|----|----|-----|-----|-----|----|----|----|-----|-----|----|
| O | 25 | 28 | 3 | 21 | 31 | 29 | - | 27 | 28 | 26 | 32 | 32 | 28 |
| Si | - | - | - | 2 | 1 | - | - | 1 | - | - | - | 1 | 24 |
| Cr | 30 | 33 | 4 | 29 | 48 | 34 | 4 | 33 | 44 | 43 | 24 | 68 | 8 |
| Mn | - | - | - | - | - | 1 | - | 1 | - | - | 3 | - | - |
| Fe | 45 | 42 | 49 | 37 | 31 | 35 | 31 | 35 | 28 | 25 | 39 | 1 | 35 |
| Ni | - | - | 43 | 8 | - | 2 | 65 | - | - | - | 6 | - | 3 |
| Total | 100 | 103 | 99 | 98 | 110 | 101 | 100 | 97 | 99 | 94 | 104 | 102 | 99 |

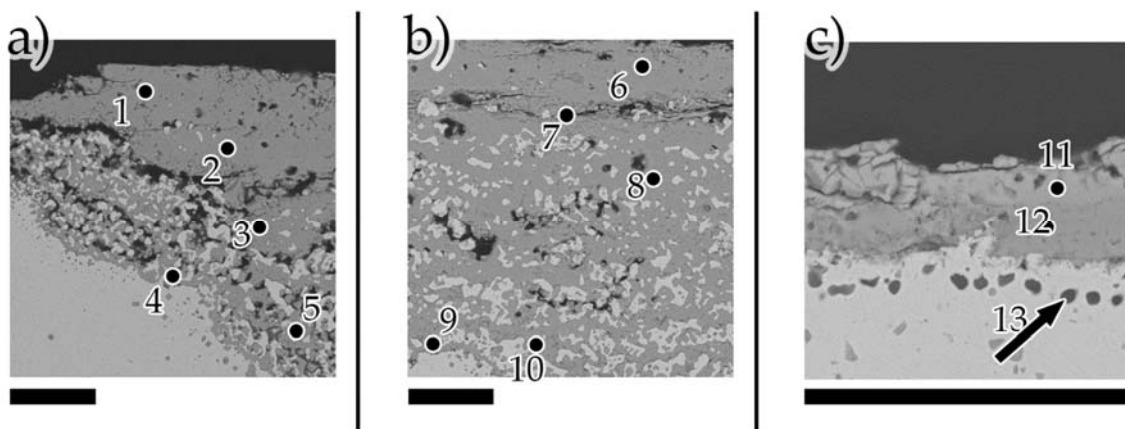


Figure 14. EDS point analysis locations in 1275 °C, (a) air, (b) oxyfuel and (c) lean oxyfuel atmospheres. Scale bar is 25 μ m.

The main morphological areas within the inner oxide layer can be observed. For samples where the oxidation progressed further, near the sample surface (e.g., analysis points 1 and 6) a CrFe oxide layer could be found directly near the original sample surface. Where the oxidation was less progressed, this layer exhibited the behaviour depicted by analysis points 11 and 12: near the oxidised sample surface a dual layer consisting of high Fe and Cr content on top, and high Cr content below. The higher Cr content layer was the Cr_2O_3 layer protecting the steel from breakaway oxidation. Analysis point 13 shows oxide nodules rich in Si forming below the protective Cr_2O_3 layer. These oxide nodules high in Si content were found to be smaller and have a lower Si content when the Cr_2O_3 layer was broken. The remnant Cr_2O_3 layer, in analysis points 4 and 9, showed an increased Fe content, very close to the levels of the top part of the dual layer, e.g., in the lean oxyfuel atmosphere at 1275 °C.

4. Discussion

For morphology, the oxidation can be considered as a continuous process, the rate of which is defined by the temperature, atmosphere and time. Morphology is the end result of the point at which this process is halted. As the time period and per-temperature heating curves were constant, atmosphere is the only variable in the function defining the severity level of the oxidation. As such, a schematic representation between the relative severity of oxidation between all temperatures and atmospheres, and the corresponding constituents to the morphology, are presented in Figure 15. The relativity between the samples is based on the ratio of the depth of the inner oxide layer and the end scaling amount. When the severity of oxidation increases, the likelihood of the left-side group constituents decreases, and the likelihood of the right-side constituents increases.

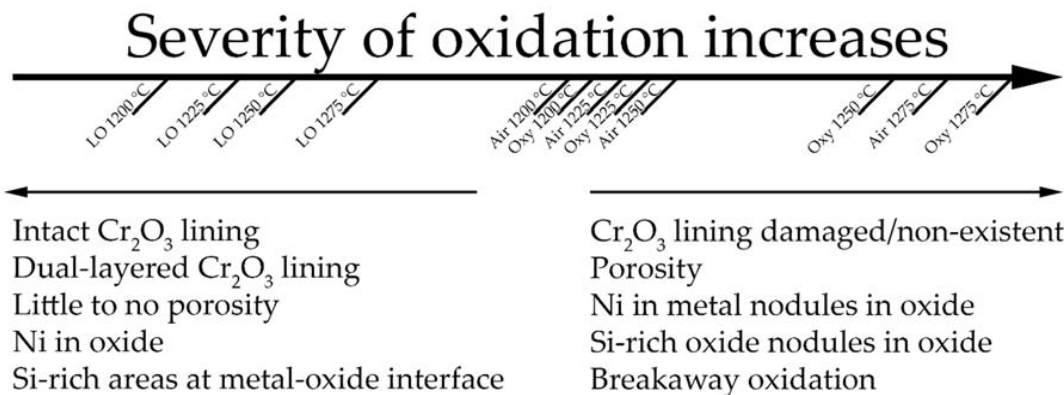


Figure 15. Relative severity of oxidation per atmosphere and temperature. The defining morphological constituents are described and the likelihood of their appearance is denoted by the arrow above the constituent groups. LO = lean oxyfuel, Oxy = oxyfuel, air = air atmosphere.

The overall TG result differences between the air atmosphere and oxyfuel atmosphere for any given temperature were rather small, as can be observed by their relative severity of oxidation in Figure 15. The differences can be seen to increase when temperature increases towards 1275 °C. Solely comparing the end scaling amounts for air versus oxyfuel atmosphere, the effect from the increased H₂O content in the oxyfuel atmosphere seems to have the same effect as a temperature increase of 25 °C in the air atmosphere. Similarly, the complete absence of oxygen in the simulated post-burn atmosphere of the lean oxyfuel atmosphere decreases the end scaling amount to around a third from that of the corresponding oxyfuel atmosphere.

Previous studies have used varying O content amounts [35,36] to determine the oxide layer thickness from GDOES results. Values between 2 and 5 wt. % have been used but only in instances where the oxide layer thickness has been between 0.5 to 20 μm thick. The TG results showed mostly sigmoidal curve shapes with an initially slow oxidation rate, followed by a period of high oxidation rate, lastly settling to a slow oxidation rate. Clear differences to other temperatures in a single atmosphere were displayed by the results in 1275 °C in all atmospheres and additionally at 1250 °C for the oxyfuel atmosphere, where the sigmoidal shape was not maintained, and the onset of breakaway oxidation could be seen starting to happen as a continuously linear high oxidation rate after the initial slow rate, or as another accelerated oxidation rate after a slight period of a slow rate. As per Wagner's [37] model for oxidation, even with its limitations [38,39], the thickness of the internal oxide layers depends on the oxygen pressure. At 1275 °C, versus other temperatures, the rate of oxidation has increased, and the thickness has also started to increase significantly, contributing to an increase in the severity of the oxidation depicted in Figure 15. Additionally, the Cr depth GDOES result at 1275 °C for air clearly shows that Cr shows a gradual decline to the alloying amount from the initially high amount at the surface, whereas lower temperatures display a steeper plummet towards the alloying amount. This would indicate that a steep descent is tied to a more protective Cr₂O₃ layer inhibiting the ion diffusion, thus hindering the growth of the oxide layer and being the rate-controlling step. The lean oxyfuel atmosphere's only source of oxygen is from the dissolved oxygen in the deionized water. As such, the oxygen partial pressure for it is much lower than for the air or oxyfuel atmospheres. The TG results and FESEM morphology images clearly show the protective capabilities of a continuous Cr₂O₃ layer, demonstrating that the oxidation has not progressed even to a stage where oxide pockets would abundantly form. Whereas the fed amount of oxygen for the air and oxyfuel atmosphere is similar, the oxyfuel atmosphere has a higher oxygen content due to the dissolved oxygen in the increased water vapor flow amount. Consequently, the oxyfuel atmosphere displayed the oxidation progressing further; either the dissolved oxygen in the increased water vapor amount was enough to contribute this increase wholly, or the substrate and oxide layer constituent reactions with H₂O also played a part. Other research has shown that in lower temperatures, an H₂O increase in the atmosphere also reduced the time it took for breakaway oxidation to start to happen for high Cr [40,41], and high CrNi Fe alloys [41] as a result of a more Cr depleted metal substrate below the oxide layer [41–43]. The TG results from this research also show that even for anisothermal oxidation practice, the oxidation rate increases happened earlier for the oxyfuel (higher H₂O content) atmosphere than they did for the air atmosphere.

The oxide layer morphology and, thus, the thickness between the oxide layers formed in high temperatures for short times versus long times are wildly different, thus the 100 ppm oxygen limit is more appropriate for use here in defining where the internal oxide layer ends and the substrate metal begins. The reason is seen from the overview images in Figure 3. Where the oxide layer is not fully propagated horizontally, the oxide pockets' bottoms are not in line with each other and the surrounding substrate matrix. As the sputtering diameter for the GDOES plasma is 4 mm, using 100 ppm as the O limit ensures that while there are probably a few pockets going deeper than the limit, at the same time there is some overhead for measurement variance and possible outliers. The GDOES results showed that

the most obvious differences between the atmospheres in a given temperature are seen between the Cr, Ni and Si contents and behaviours as a function of the sample depth. The combined TG and GDOES results at 1200 °C, 1225 °C and 1250 °C in the air atmosphere show a peculiar behaviour for the high temperature oxidation. The TG graphs, seen in Figure 4, show that at 1200 °C, the total normalised oxide formation amount is momentarily higher than at 1225 °C between 7400 and 8400 s. Additionally, the Ni GDOES depth profile showed that the overall Ni concentration of the 1225 °C temperature sample is the lowest of the air atmospheres in addition to the Cr GDOES depth profile, showing that the decline to the substrate concentration happens at the lowest depth for 1225 °C.

Porosity in the samples was affected by the thickness of the inner oxide layer. The further the oxidation had progressed, the higher the porosity. A major part of porosity not originating from cracking in the oxide layer is the result of the formed Ni-rich particles in the inner oxide layer. For example, in Figure 13a FESEM BSE image, it can be seen that the porosity differences in the upper and lower part of the inner oxide layer differ quite a lot. Seen from the Ni-EDS map for the same image, the Ni-rich particles have formed at the bottom of the inner oxide layer, but not at the upper parts. Subsequently, porosity is higher in the lower part of the inner oxide layer than it is in the upper part. Comparing Figure 13a to b, it is shown that in (b), the Ni-rich particles are found throughout the inner oxide layer, and the porosity is more uniform than in (a). Further comparing both Figure 13a,b to c, it is seen that for the lean oxyfuel atmosphere, pores are quite large, but there are only a few of them. The way the oxide layer forms to the steel studied is through the formation of oxide pockets, the growth of these pockets, width- and depth-wise, and finally to the uniform layer which makes the porosity dependent on the general progressivity phase of this evolution; that is, porosity in general for any sample in any temperature can be gauged by averaging the porosity in all pockets throughout the sample surface. As such, the general level of porosity is smaller in the lean oxyfuel atmosphere samples due to a smaller number of oxide pockets in a phase where all of the Ni in the oxide has progressed to Ni-rich particles. The porosity of air and oxyfuel atmospheres were comparable at a general level. As the oxide formation amount was much lower in the lean oxyfuel atmosphere, little to no porosity was observed.

The Ni depth profiles for the oxyfuel atmosphere's 1200 °C and 1225 °C samples were very close to each other. However, for the air atmosphere, the 1200 °C Ni depth profile was very close to the one for 1250 °C. Considering all this, the 1250 °C temperature at the air atmosphere is similarly different from what the 1225 °C temperature is in the oxyfuel atmosphere. Both exhibit a high Si content near the original sample surface and come closer to their one 25 °C step below the TG result than the same step higher. The occurrence of the Ni-particles in the inner oxide layer is linked to the Cr₂O₃ lining at the metal/oxide interface starting to dissipate. This is evident from Figure 16: from the oxyfuel sample at 1225 °C, it depicts the BSE, Ni, Cr and Si EDS maps of the sample. Observing the image, it can be seen that to the left of the vertical purple line, the Cr₂O₃ is intact, with minimal Ni particles inside the inner oxide layer above the lining. To the right side of the purple vertical line and directly below the lining, seen as darker areas in contrast to the same position on the left, the Cr content can be seen to have diminished at the metal substrate. Additionally, Ni particles now appear in wave-like patterns in the cross-section of the sample. The composition of the Ni particles, with varying ratios of Ni and Fe, up to 90 wt. % of Ni and 3 wt. % of Cr, would place it as γ -(Fe,Ni) with diluted Cr [44,45].

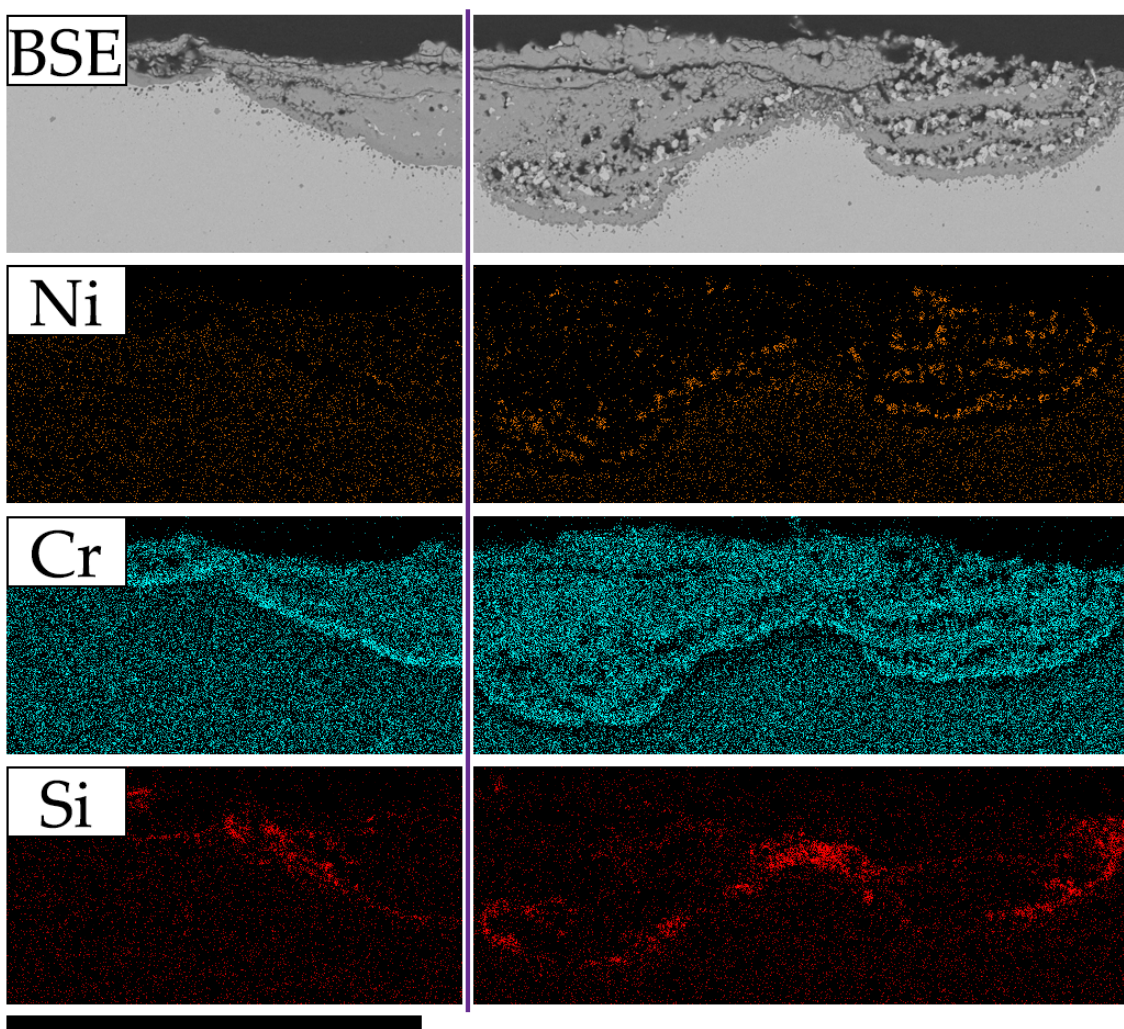


Figure 16. BSE, Ni, Cr and Si EDS maps from the sample 1225 °C in oxyfuel atmosphere. Scale bar is 100 μm .

The Si-rich oxide nodules below the Cr_2O_3 layer at the oxide–metal interface can be seen to be larger to the left of the purple line in Figure 16 where oxidation has not progressed to the point of the weakened/broken Cr_2O_3 layer. Additionally, their appearance in the BSE image is darker, while the Si EDS map shows the localisation of Si content to be more clustered near the oxide/metal interface to the left of the purple line as well. Zheng et al. [46] have proposed that the non-uniform distribution of the Si-rich oxide phase inside the inner oxide layer could be the result of the inward movement of Fe_2SiO_4 . They additionally propose that for a single Si-rich nodule, or in their case an Fe_2SiO_4 nodule, a single nodule observes oxidation of the nodule at the gas interface side, the formation of Fe_2SiO_4 on the steel substrate side, and Si diffusion towards the substrate side inside the nodule. Observing the Si EDS map in Figure 16; to the left of the purple line, the Si in the inner oxide layer shows higher amounts of Si near the Cr_2O_3 lining at the metal/oxide interface. However, to the right, the Si is additionally localised next to the formed Ni-rich metal nodules with a high number of pores next to them. The formation of pores next to the Si-rich oxide areas may be the result of Kirkendall porosity [47], supporting the Fe_2SiO_4 diffusion. However, should the porosity originate from Fe_2SiO_4 diffusion, it would either require (1) whole Fe_2SiO_4 nodules diffusing, along with the already diffusing O^- and Fe^+ surrounding the nodules or (2) the diffusion speed and speed difference between the already diffusing species to increase. In any case, the breaking of the Cr_2O_3 lining at the metal/oxide interface is linked to triggering the event as is seen in the Figure 16 Cr EDS map; the Cr content to the right of the purple line is lower at the metal/oxide interface.

Combining the EDS and GDOES results, the differences between the air and oxyfuel atmospheres' morphologies for Ni, Si and Cr distribution, depth wise, are inherently linked to the scale growth amount itself. Thus, per temperature, there are differences between the behaviour of these elements' depth profiles and morphology contributions, but the differences seem to be because of the point the oxidation has progressed to, not implicitly because of the atmosphere. However, the point to which the oxidation has progressed to is because of the atmosphere.

All considered, the overall effect from using oxyfuel practice, and thus oxygen as the oxidiser in comparison to air atmosphere, was a clear impact on the amount of formed oxide. The increased H₂O content in the simulated post-burn atmosphere for the oxyfuel atmosphere at a single temperature versus the air atmosphere had the equivalent effect on the oxide scale formation amount as increasing the temperature by 25 °C in the air atmosphere. Simulating a lean burn oxyfuel atmosphere, the effect of not having oxygen in the atmosphere had a major impact on negating the formed oxide scale amount when compared to the regular simulated oxyfuel post-burn atmosphere. Thus, the role of a significantly increased H₂O content has a lower effect on the end scaling amount at each temperature than having no free oxygen and having 3.22 vol. % free oxygen.

5. Conclusions

The following conclusions were drawn from the research comparing AISI 304 stainless steel oxide formation characteristics in a simulated post-burn atmosphere where air, oxyfuel and lean oxyfuel were used as the oxidisers to the burn reaction:

- The lean oxyfuel atmosphere led to the lowest amount of formed oxide scale, followed by the air atmosphere and then the oxyfuel atmosphere. The differences in scale formation amounts between the lean oxyfuel atmosphere and air were much greater than between the air and oxyfuel atmosphere.
- The effect of switching from the air atmosphere to oxyfuel atmosphere in a single temperature is proportional to a 25 °C temperature increase in the air atmosphere from the scale formation amount's perspective. The effect of switching to a lean oxyfuel atmosphere from an oxyfuel atmosphere is a drop to a third of the scale formation amount.
- The inner oxide layers' penetration depth order from the lowest depth to the greatest depth was the same: lean oxyfuel, air and oxyfuel at any single temperature between the atmospheres.
- A GDOES analysis revealed differences in the Ni, Si and Cr content behaviour in relation to the depth between a single atmosphere's multiple temperatures and between a single temperature and multiple atmospheres.
- A FESEM/EDS analysis revealed a link between the intactness of the Cr₂O₃ lining at the substrate/oxide interface and the formation of Ni-rich particles in the inner oxide layer, as well as to the disappearance of Si-rich oxide nodules below the lining in the substrate.
- A substantial increase in the H₂O content has a lower effect on the total oxide scale formation amount than a slight increase in the free oxygen content in a situation where there is no free oxygen.

Author Contributions: Methodology, validation, formal analysis, investigation, resources, data curation, writing—original draft preparation, visualisation: A.L. Conceptualisation, writing—review and editing: A.L., E.-P.H., T.F. All authors have read and agreed to the published version of the manuscript.

Funding: This research received no external funding.

Acknowledgments: This research is a part of Business Finland funded Towards Carbon Neutral Metals (TOCANEM) project. The authors wish to thank the project partners involved in the research and the staff of the process metallurgy group in the University of Oulu.

Conflicts of Interest: The authors declare no conflict of interest.

References

1. Abuluwafa, H.T.; Guthrie, R.I.L.; Ajersch, F. Oxidation of low carbon steel in multicomponent gases: Part II. Reaction mechanisms during reheating. *Metall. Mater. Trans. A* **1997**, *28*, 1643–1651. [[CrossRef](#)]
2. Niska, J.; Grip, C.-E.; Mellin, P. Investigating Potential Problems and Solutions of Renewable Fuel Use in Steel Reheating Furnaces. In Proceedings of the Conference proceedings of Finnish—Swedish Flame Days 2013, Jyväskylä, Finland, 17–18 April 2013.
3. Orsino, S.; Weber, R.; Bollettini, U. Numerical simulation of combustion of natural gas with high-temperature air. *Combust. Sci. Technol.* **2001**, *170*, 1–34. [[CrossRef](#)]
4. da Costa, F.C. Fuel Gas Applications in Industry. *Handb. Combust.* **2010**, *3*, 237–264. [[CrossRef](#)]
5. Han, S.H.; Chang, D. Radiative slab heating analysis for various fuel gas compositions in an axial-fired reheating furnace. *Int. J. Heat Mass Transf.* **2012**, *55*, 4029–4036. [[CrossRef](#)]
6. Mariños Rosado, D.J.; Rojas Chávez, S.B.; Amaro Gutierrez, J.; Mayworm de Araújo, F.H.; de Carvalho, J.A.; Mendiburu, A.Z. Energetic analysis of reheating furnaces in the combustion of coke oven gas, Linz-Donawitz gas and blast furnace gas in the steel industry. *Appl. Therm. Eng.* **2020**, *169*, 114905. [[CrossRef](#)]
7. Lee, D.B.; Choi, J.W. High temperature oxidation of steels in air and CO₂-O₂ atmosphere. *Oxid. Met.* **2005**, *64*, 319–329. [[CrossRef](#)]
8. Balbis, L.; Balderud, J.; Grimble, M.J. Nonlinear predictive control of steel slab reheating furnace. In Proceedings of the 2008 American Control Conference, Seattle, WA, USA, 11–13 June 2008; pp. 1679–1684. [[CrossRef](#)]
9. Oliveira, F.A.D.; Carvalho, J.A.; Sobrinho, P.M.; de Castro, A. Analysis of oxy-fuel combustion as an alternative to combustion with air in metal reheating furnaces. *Energy* **2014**, *78*, 290–297. [[CrossRef](#)]
10. Lindell, D.; Ekman, T.; Pettersson, R. Fast and efficient annealing of stainless steel strip using oxyfuel burners. *Steel Res. Int.* **2015**, *86*, 557–566. [[CrossRef](#)]
11. Riley, M.F.; Kobayashi, H.; Deneys, A.C. Praxair’s dilute oxygen combustion technology for pyrometallurgical applications. *JOM* **2001**, *53*, 21–24. [[CrossRef](#)]
12. Heil, P.; Toporov, D.; Förster, M.; Kneer, R. Experimental investigation on the effect of O₂ and CO₂ on burning rates during oxyfuel combustion of methane. *Proc. Combust. Inst.* **2011**, *33*, 3407–3413. [[CrossRef](#)]
13. Corna, N.; Dentella, F. Recent developments in the application of Oxygen combustion to ladle preheating stations and steel reheating furnaces. *Metall. Ital.* **2011**, *103*, 33–38.
14. Saha, C.; Ganguly, R.; Datta, A. Heat transfer and emission characteristics of impinging rich methane and ethylene jet flames. *Exp. Heat Transf.* **2008**, *21*, 169–187. [[CrossRef](#)]
15. Malikov, G.; Lisienko, V.; Malikov, Y.; Wagner, J.; Kurek, H.; Chudnovsky, Y.; Viskanta, R. Mathematical modeling of direct flame impingement heat transfer. *ASME Int. Mech. Eng. Congr. Expo. HTD* **2006**, *47845*, 615–623. [[CrossRef](#)]
16. Sánchez, M.; Cadavid, F.; Amell, A. Experimental evaluation of a 20kW oxygen enhanced self-regenerative burner operated in flameless combustion mode. *Appl. Energy* **2013**, *111*, 240–246. [[CrossRef](#)]
17. Fry, A.; Adams, B.; Paschedag, A.; Kazalski, P.; Carney, C.; Oryshchyn, D.; Woodside, R.; Gerdemann, S.; Ochs, T. Principles for retrofitting coal burners for oxy-combustion. *Int. J. Greenh. Gas Control* **2011**, *5*, S151–S158. [[CrossRef](#)]
18. Malikov, G.K.; Lobanov, D.L.; Malikov, K.Y.; Lisienko, V.G.; Viskanta, R.; Fedorov, A.G. Direct flame impingement heating for rapid thermal materials processing. *Int. J. Heat Mass Transf.* **2001**, *44*, 1751–1758. [[CrossRef](#)]
19. Kim, M.Y. A heat transfer model for the analysis of transient heating of the slab in a direct-fired walking beam type reheating furnace. *Int. J. Heat Mass Transf.* **2007**, *50*, 3740–3748. [[CrossRef](#)]
20. Pronk, P.; Boeder, C.J.; Bsibsi, M.; Luinenburg, A.; Speets, R.; Staelman, D.; Verhoeft, R.; Wu, H. Advances in control of thermal processes in steel rolling mills of Tata Steel. In Proceedings of the ROLLING Conference 2016, Graz, Austria, 6–9 June 2016.
21. Han, S.H.; Chang, D.; Kim, C.Y. A numerical analysis of slab heating characteristics in a walking beam type reheating furnace. *Int. J. Heat Mass Transf.* **2010**, *53*, 3855–3861. [[CrossRef](#)]
22. Huenert, D.; Kranzmann, A. Impact of oxyfuel atmospheres H₂O/CO₂/O₂ and H₂O/CO₂ on the oxidation of ferritic-martensitic and austenitic steels. *Corros. Sci.* **2011**, *53*, 2306–2317. [[CrossRef](#)]
23. Saunders, S.R.J.; Monteiro, M.; Rizzo, F. The oxidation behaviour of metals and alloys at high temperatures in atmospheres containing water vapour: A review. *Prog. Mater. Sci.* **2008**, *53*, 775–837. [[CrossRef](#)]
24. Paneru, M.; Stein-Brzozowska, G.; Maier, J.; Scheffknecht, G. Corrosion mechanism of alloy 310 austenitic steel beneath NaCl deposit under varying SO₂ concentrations in an oxy-fuel combustion atmosphere. *Energy Fuels* **2013**, *27*, 5699–5705. [[CrossRef](#)]
25. Meier, G.H.; Jung, K.; Mu, N.; Yanar, N.M.; Pettit, F.S.; Pirón Abellán, J.; Olszewski, T.; Nieto Hierro, L.; Quadakkers, W.J.; Holcomb, G.R. Effect of alloy composition and exposure conditions on the selective oxidation behavior of ferritic Fe-Cr and Fe-Cr-X alloys. *Oxid. Met.* **2010**, *74*, 319–340. [[CrossRef](#)]
26. Chandra, K.; Kranzmann, A.; Saliwan Neumann, R.; Oder, G.; Rizzo, F. High Temperature Oxidation Behavior of 9–12% Cr Ferritic/Martensitic Steels in a Simulated Dry Oxyfuel Environment. *Oxid. Met.* **2015**, *83*, 291–316. [[CrossRef](#)]
27. Chandra, K.; Dörfel, I.; Wollschläger, N.; Kranzmann, A. Microstructural investigation using advanced TEM techniques of inner oxide layers formed on T92 steel in oxyfuel environment. *Corros. Sci.* **2019**, *148*, 94–109. [[CrossRef](#)]
28. Huczkowski, P.; Najima, S.; Chyrkin, A.; Quadakkers, W.J. Corrosion Behavior of Austenitic Stainless Steels in Oxidizing and Reducing Gases Relevant to Oxyfuel Power Plants. *JOM* **2018**, *70*, 1502–1510. [[CrossRef](#)]

29. Pirón Abellán, J.; Olszewski, T.; Penkalla, H.J.; Meier, G.H.; Singheiser, L.; Quadakkers, W.J. Scale formation mechanisms of martensitic steels in high CO₂/H₂O-containing gases simulating oxyfuel environments. *Mater. High Temp.* **2009**, *26*, 63–72. [[CrossRef](#)]
30. Ani, M.H.B.; Kodama, T.; Ueda, M.; Kawamura, K.; Maruyama, T. The effect of water vapor on high temperature oxidation of Fe-Cr alloys at 1073 K. *Mater. Trans.* **2009**, *50*, 2656–2663. [[CrossRef](#)]
31. Bleck, W.; Heidelauf, T.; Meyer, L.; Straburger, C.; Wolpert, W.; Zimmer, W. Effect of temperature sequence during hot strip rolling on structure and properties of mild steels. *Steel Res.* **1993**, *64*, 396–400. [[CrossRef](#)]
32. Hoile, S. Processing and properties of mild interstitial free steels. *Mater. Sci. Technol.* **2000**, *16*, 1079–1093. [[CrossRef](#)]
33. Lee, H.; Park, K.S.; Lee, J.H.; Heo, Y.U.; Suh, D.W.; Bhadeshia, H.K.D.H. Dissolution behaviour of NbC during slab reheating. *ISIJ Int.* **2014**, *54*, 1677–1681. [[CrossRef](#)]
34. Landfahrer, M.; Schluckner, C.; Gerhardt, H.; Zmek, T.; Klarner, J.; Hochenauer, C. Numerical model incorporating different oxidizer in a reheating furnace fired with natural gas. *Fuel* **2020**, *268*, 117185. [[CrossRef](#)]
35. Lindell, D.; Pettersson, R. Pickling of Process-Oxidised Austenitic Stainless Steels in HNO₃-HF Mixed Acid. *Steel Res. Int.* **2010**, *81*, 542–551. [[CrossRef](#)]
36. Elger, R.; Pettersson, R. Effect of Addition of 4% Al on the High Temperature Oxidation and Nitridation of a 20Cr–25Ni Austenitic Stainless Steel. *Oxid. Met.* **2014**, *82*, 469–490. [[CrossRef](#)]
37. Wagner, C. Reaktionstypen bei der Oxydation von Legierungen. *Z. Elektrochem. Ber. Bunsenges. Phys. Chem.* **1959**, *63*, 772–782. [[CrossRef](#)]
38. Morin, F.; Beranger, G.; Lacombe, P. Limits of application for Wagner's oxidation theory. *Oxid. Met.* **1972**, *4*, 51–62. [[CrossRef](#)]
39. Douglass, D.L. A critique of internal oxidation in alloys during the post-wagner era. *Oxid. Met.* **1995**, *44*, 81–111. [[CrossRef](#)]
40. Othman, N.K.; Zhang, J.; Young, D.J. Temperature and water vapour effects on the cyclic oxidation behaviour of Fe-Cr alloys. *Corros. Sci.* **2010**, *52*, 2827–2836. [[CrossRef](#)]
41. Nguyen, T.D.; Zhang, J.; Young, D.J. Water vapour effects on corrosion of Fe-Cr and Fe-Cr-Ni alloys containing cerium and manganese in CO₂ gas at 818 °C. *Corros. Sci.* **2014**, *89*, 220–235. [[CrossRef](#)]
42. Jonsson, T.; Larsson, H.; Karlsson, S.; Hooshyar, H.; Sattari, M.; Liske, J.; Svensson, J.E.; Johansson, L.G. High-Temperature Oxidation of FeCr(Ni) Alloys: The Behaviour After Breakaway. *Oxid. Met.* **2017**, *87*, 333–341. [[CrossRef](#)]
43. Jonsson, T.; Karlsson, S.; Hooshyar, H.; Sattari, M.; Liske, J.; Svensson, J.E.; Johansson, L.G. Oxidation After Breakdown of the Chromium-Rich Scale on Stainless Steels at High Temperature: Internal Oxidation. *Oxid. Met.* **2016**, *85*, 509–536. [[CrossRef](#)]
44. Mills, K.C. *Slag Atlas*, 2nd ed.; Verlag Stahleisen GmbH: Düsseldorf, Germany, 1995; ISBN 3514004579.
45. Singh, N.; Pandey, V.; Srivastava, G.; Banerjee, S.; Parkash, O.; Kumar, D. γ and α -(Fe, Ni) phase characterization using image processing and effect of phase formation on the P/M Fe(100-x)Ni(x) alloys properties. *Mater. Chem. Phys.* **2020**, *246*, 122794. [[CrossRef](#)]
46. Zheng, L.; Hosoi, K.; Ueda, S.; Gao, X.; Kitamura, S.Y.; Kobayashi, Y. Si-rich phases and their distributions in the oxide scale formed on 304 stainless steel at high temperatures. *J. Nucl. Mater.* **2018**, *507*, 327–338. [[CrossRef](#)]
47. Seitz, F. On the porosity observed in the Kirkendall effect. *Acta Metall.* **1953**, *1*, 355–369. [[CrossRef](#)]